On uncertainty in fusion neutronics

Fred Thomas

Department of Physics
University of York

This dissertation is submitted for the degree of
Doctor of Philosophy

September 2018

I would like to dedicate this thesis to my loving parents …

Declaration

I hereby declare that except where specific reference is made to the work of others, the contents of this dissertation are original and have not been submitted in whole or in part for consideration for any other degree or qualification in this, or any other university. This dissertation is my own work and contains nothing which is the outcome of work done in collaboration with others, except as specified in the text and Acknowledgements. This dissertation contains fewer than 65,000 words including appendices, bibliography, footnotes, tables and equations and has fewer than 150 figures.

Fred Thomas
September 2018

Acknowledgements

And I would like to acknowledge ...

Many thanks to Michael Loughlin for his advice and arranging the research placement at ITER Organisation in Provence, France. Jakhar Shrichand and Vladimir Barabash also of ITER were a great help. This work was supported by the Engineering and Physical Sciences Research Council [EP/L01663X/1].

The authors would like to thank to Igor Lengar for sharing his model of the LTIS foil holder with us. Also, to Beth Colling, Steve Bradnam and Jon Naish for helpful conversations concerning JET and LTIS. This work was funded by the Engineering and Physical Sciences Research Council [EP/L01663X/1] via the Fusion Centre for Doctoral Training (FCDT).

This work was supported by the Engineering and Physical Sciences Research Council (EPSRC) [EP/L01663X/1].

Abstract

This is where you write your abstract ...

Table of contents

List of figures **xiii**

List of tables **xvii**

Nomenclature **xix**

1 Background **1**
  1.1 Nuclear fusion 1
  1.2 Neutron-matter interactions 1
  1.3 Sources of uncertainty in fusion neutronics 1
  1.4 Implications of current uncertainties 1
  1.5 Thesis outline 1

2 Total Monte Carlo propagation of nuclear data uncertainties to nuclear fusion engineering parameters **3**
  2.1 Introduction 3
  2.2 Method 5
  2.3 Input nuclear data 6
  2.4 Results & discussion 7
  2.5 Conclusion 8

3 Quantifying received dose errors introduced by spatial homogenisation of reinforced concrete shielding **13**
  3.1 Introduction 13
  3.2 Method 14
    3.2.1 Prompt neutron & gamma radiation 14
    3.2.2 Delayed gamma radiation 15
  3.3 Results & discussion 17
    3.3.1 Transmission of prompt radiation 17

3.3.2 Shut Down Dose Rate 17
3.4 Conclusion 20

4 Optimising energy group structures for neutron activation calculations in fusion systems 27
4.1 Outline 27
4.2 Introduction 27
4.3 Method 29
4.3.1 Reactions 30
4.3.2 Group structure optimisation 30
4.3.3 Radiation transport 32
4.4 Results & Discussion 33
4.5 Conclusions 34

5 Concluding remarks 43
5.1 Comparison of sources of uncertainty studied 43
5.2 Recommendations for neutronics practitioners 43
5.3 Recommendations for further research 43

References 45

List of figures

2.1 Shown here are ^{208}Pb (n,2n) cross-sections as a function of energy. The plot shows the TENDL 'random' data extracted from ACE files. Additionally, the few available experimental results in EXFOR are plotted for comparison. 5

2.2 Shown are histograms of $\sigma_{n,2n}$ at 14MeV for the three major Pb isotopes. It can be seen that while ^{206,208}Pb are approximately symmetrical with skewness values close to zero, ^{207}Pb has a skewness of -0.868 indicating a low-value tail. This may or may not be representative of the underlying distribution. The histogram contains all 300 available files for ^{207}Pb, but it could be the case that with more files a Gaussian shape would be recovered. 7

2.3 The elastic scattering cross-sections for lead at 14MeV are all positively skewed, with ^{208}Pb having a skewness value of 1.185. 8

2.4 Shown here are scatter plots of the relationship between the scattering and n,2n cross-sections in the TENDL data. The two channels are clearly anti-correlated. A least squares fit has been applied and the resulting linear relationship plotted. 9

2.5 The mean and standard deviation of the TBR distribution is presented as a function of the number of simulations. The TMC simulation can be seen to converge at approximately 400 MCNP runs. $\mu(400) \approx 1.02$ and $\sigma(400) \approx 1.14$. 10

2.6 Above are scatter plots of average cross-sections for the n,2n (left) and elastic (right) channels against resulting TBR value. As the cross-sections for each of the three lead isotopes were varied in every simulation, so the cross-sections plotted here are the elemental average values denoted as $\bar{\sigma}_{n,2n}$ or $\bar{\sigma}_{n,n'}$, i.e. all three varied Pb isotopes contribute, weighted by their relative natural abundances. The n,2n cross-section is positively correlated with the TBR value as expected. There is less of a relationship between scattering and TBR. 10

2.7 Histogram of TBR values computed with the TMC methodology. 11

3.1 The two modelling approaches considered in this investigation. a) Heterogeneous, where the steel reinforcing bar and stirrups are explicitly modelled. b) Homogeneous, where the mass of rebar is 'smeared' through the concrete. The new homogenised material has a greater density than plain concrete, conserving mass. 16
3.2 Neutron spectra for incident radiation. This spectra was recorded in 175 energy groups from the back of the ITER Neutral Beam assembly, immediately inside the bioshield concrete wall. 16
3.3 The flux to dose conversion factors for neutron and photon exposure. 18
3.4 The neutron spectra leaving the shield for the heterogeneous and homogeneously modelled cases. Note the substantially reduced thermal flux in the homogeneous simulation. This spectrum has been binned with a finer energy grid than the source, the TRIPOLI 315 group structure. 18
3.5 The nuclear properties of steel and concrete are substantially different. Shown here is the cross-section for (n,γ) in both materials. 19
3.6 The homogeneous flux increases are readily visible here. 21
3.7 The discrepancy between modelling approaches is a function of the wall thickness for thin walls. 22
3.8 The total ϕ_γ as a function of cooling time. The homogeneous simulation gives a significantly increased value at time steps beyond $10^5 s$ or approximately 1 day. 23
3.9 The path lengths of neutrons in pure concrete are shown as a histogram. There is a wide distribution with a mean of approximately 2cm. 24
3.10 This plot shows an estimate for the specific contact dose rate due to steel and concrete irradiated under the ITER SA-2 scenario. Nuclides which contribute a significant fraction of the dose are shown with their abscissa value as their half-life, $t_{\frac{1}{2}}$. 25

4.1 Shown in the upper plot is a ^{186}W radiative capture reaction rate, both unshielded and shielded. The incident particle spectrum in this case is a power function of energy, i.e. $\phi(E) = E^x$ where x is some constant. The second plot shows the calculated self-shielding factors as a function of energy for this reaction, given an elemental material composition. The third and fourth plots are derived quantities used for group structure optimisation. See section 4.3.2 for more details. 35

4.2 Typical DT neutron spectrum within the LTIS activation foil holder. The fluence of each bin has been divided by the lethargy width for that bin, ΔU. The spectrum is hard, with little thermalisation as a consequence the foil's proximity to the plasma. The same neutrons have been binned according to various group structures, from 175 to 709 groups. 36
4.3 Magnified section of spectrum showing how progressively finer group structures resolve flux depressions in a neutron spectrum. 37
4.4 Comparison of different calculation methods for radiative capture in ^{182}W under JET neutron irradiation. 38
4.5 Comparison of different calculation methods for radiative capture in ^{186}W under JET neutron irradiation. 39
4.6 Comparison of different calculation methods for radiative capture in ^{181}Ta under JET neutron irradiation. 40
4.7 Comparison of different calculation methods for radiative capture in ^{95}Mo under JET neutron irradiation. 41

List of tables

2.1 Cross-section values for the n,2n reaction channel, $\sigma_{n,2n}$ around 14 MeV for various libraries and experiments. The ENDF utility code Inter [**?**] was used to extract the values for each library. The two experimental results were retreived from the online EXFOR database [**?**]. The uncertainties, $\Delta\sigma_{n,2n}$ are presented as percentages above and below the reported value. 4
2.2 TENDL2015 'random' Pb n,2n neutron multiplicity channel cross-section distribution statistics 6
2.3 TENDL2015 'random' Pb elastic scattering cross-section distribution statistics 6

4.1 Shown above are the reactions simulated in this study. $\mathrm{E}_{\text{first res.}}$ indicates the energy of the first resonant peak in the interaction cross-section. $\mathrm{E}_{\mathrm{URR}}$ defines the end of the resolved resonance range (RRR) and the start of the unresolved resonance range (URR) where experimental energy resolution is insufficient to resolve individual resonances. 30
4.2 Comparison of group structures tested, noting their bin counts, $\mathrm{n}_{\mathrm{bins}}$, the energy range over which they are defined and the bins per decade, $\mathrm{bpd}_{\mathrm{res}}$ they employ in the resonant region. 32

Nomenclature

Greek Symbols

π	$\simeq 3.14\ldots$

Chapter 1

Background

1.1 Nuclear fusion

1.2 Neutron-matter interactions

1.3 Sources of uncertainty in fusion neutronics

1.4 Implications of current uncertainties

1.5 Thesis outline

Chapter 2

Total Monte Carlo propagation of nuclear data uncertainties to nuclear fusion engineering parameters

2.1 Introduction

To sustainably liberate energy from the D-T fusion reaction requires a reliable supply of tritium fuel. Given tritium is not naturally occuring, with a $t_{\frac{1}{2}} = 12.3y$ it must be artificially produced. This is to be achieved by breeding it from ^{6,7}Li in a blanket. The ratio of tritium produced to tritium consumed, or Tritium Breeding Ratio (TBR), is required to have some margin over unity to compensate for various losses: absorption in materials, leakage in the tritium extraction system and radioactive decay. However, there is a constraint on the maximum allowable tritium inventory at a given facility on the order of kg. The window of adequate tritium supply is therefore relatively narrow and TBR should be precisely known and/or adjustable to keep within this window. A D-T fusion reactor would burn tritium at a rate of 56kg per GW_{fus} per full power year. Therefore, for a 1 GW_{e} plant a 1% TBR uncertainty would result in an inventory uncertainty of 1-2kg of tritium per year.

Unfortunately there are many sources of uncertainty within TBR calculations. These can broadly be categorised as: poor/missing nuclear data, modelling simplifications and Monte-Carlo statistical uncertainty. Nuclear data often contributes the greatest uncertainty to TBR [3]. However, the effect of these uncertainties is rarely reported alongside calculated TBR values. This is in large part due to the difficulty of propagating uncertainty data through a Monte-Carlo radiation transport simulation to the uncertainty on integral quantities of interest. Any uncertainties that are propagated are generally based on a simplified uncertainty treatment that does not include full energy, emitted double-differential and channel-to-channel correlations.

A sensitivity analysis of HCLL type breeder blankets for the ITER Test Blanket Modules (TBMs) has identified ^{6}Li, ^{56}Fe and the Pb cross-sections as the most important for TBR uncertainty [8]. This paper quantifies the TBR uncertainty introduced by Pb nuclear data on the HCLL DEMO blanket design by employing the TMC methodology.

Source	E [MeV]	$\sigma_{n,2n}$ [b]	$\pm\%\Delta\sigma_{n,2n}$
BROND 2.2	14.0	1.97	-
CENDL 3.1	14.0	2.08	-
ENDF/B-VII.1	14.0	2.22	8.15
JEFF 3.2	14.0	2.18	7.0
JENDL 4.0	14.0	2.15	10.1
TENDL 2015	14.0	2.19	7.4
RUSFOND 2010	14.0	2.18	-
EXFOR: Simakov	14.1	2.38	5.88
EXFOR: J. Frehaut	14.28	1.97	8.57

Table 2.1 Cross-section values for the n,2n reaction channel, $\sigma_{n,2n}$ around 14 MeV for various libraries and experiments. The ENDF utility code Inter [**?**] was used to extract the values for each library. The two experimental results were retreived from the online EXFOR database [**?**]. The uncertainties, $\Delta\sigma_{n,2n}$ are presented as percentages above and below the reported value.

Cross-section uncertainties can be represented as single values for a given energy and reaction channel. As an example, the ^{208}Pb(n,2n)^{207}Pb reaction at 14MeV is shown in Table 2.1 for a variety of nuclear data libraries. Information on how uncertainty for a given energy affects other energies is quantified in energy covariance matrices, but these are not available for the majority of reaction channels in standard nuclear data libraries.

The TENDL-2015 library is a comprehensive, general-purpose nuclear data library which contains data on interactions between 7 projectiles and over 2,800 target nuclides. The library is produced by a suite of codes known as T6 and an adherance to a strict methodology of reproducability [13]. It uses the TALYS nuclear reaction code to model reactions and predict nuclear data. The inputs are fundamental parameters, including data from the RIPL-3 database [**?**], each with their own probability distributions that reflect their uncertainties. For the TENDL libraries, the distribution of nuclear data contained in the files with sampled input parameters can give more information on nuclear data uncertainty than is contained in a traditional evaluated nuclear data file. The shape of the distribution are captured and need not necessarily be simple Gaussian.

The Total Monte-Carlo (TMC) method utilises nuclear data generated from these sampled fundamental parameters to quantify uncertainties on integral quantities. With a given

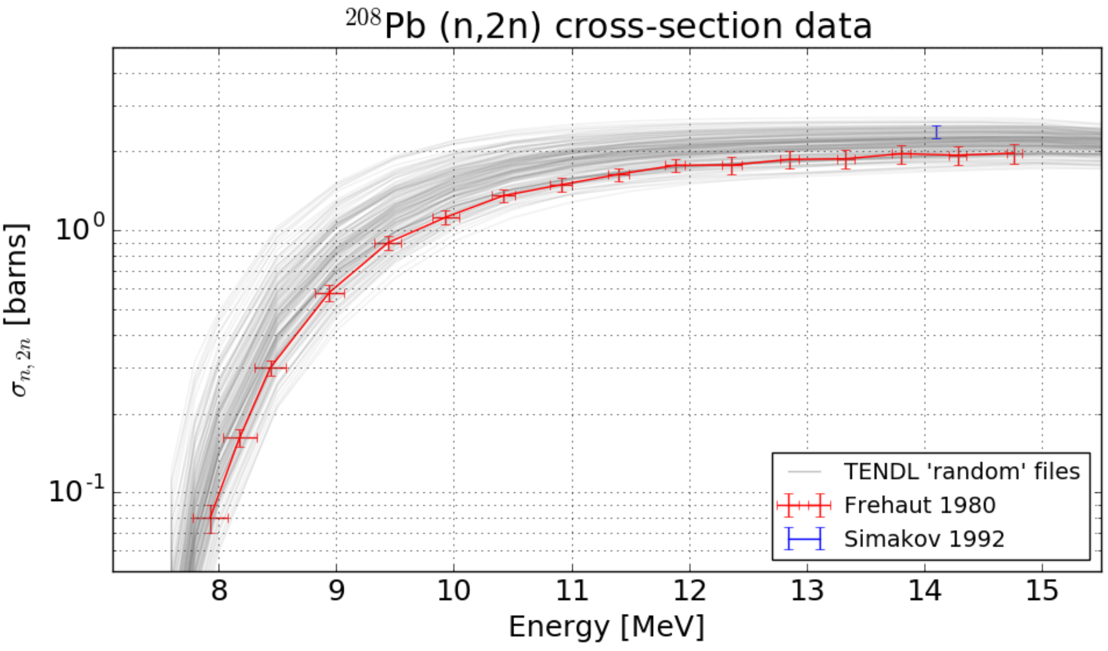

Fig. 2.1 Shown here are ^{208}Pb (n,2n) cross-sections as a function of energy. The plot shows the TENDL 'random' data extracted from ACE files. Additionally, the few available experimental results in EXFOR are plotted for comparison.

ensemble of sampled nuclear data, a radiation transport simulation is performed and an observable recorded. The process is repeated hundreds of times to produce a distribution of the observable of interest, with the uncertainty in the fundamental parameters used in the genration of self-consistent nuclear data files, propagating the fully-correlated variations to the observable PDF [7].

2.2 Method

The sampled nuclear data files were downloaded in both ACE (293K) and ENDF format from the TENDL-2015 website [**?**]. Figure 2.1 shows the (n,2n) cross-sections as a function of energy for ^{208}Pb.

The ENDF utility code Inter was used to extract cross-section values at a given energy from the ENDF files. The resulting distributions and correlations were plotted as figures 2.2, 2.3 & 2.4. Figures 2.2 and 2.3 were examined for their first 3 statistical moments.

An 11.25° 2014 DEMO HCLL MCNP model was modified to tally TBR. The particle count was set to $3 \cdot 10^6$ giving a TBR relative standard deviation, RSD ≈ 0.002 for each simulation. This is negligible compared to the total (nuclear data & statistics) accumulated

RSD and so the variance of the observable is assumed to be entirely due to variance in the nuclear data. While other TMC analyses have separated out the Monte-Carlo statistical variations to limit the computational cost [14], in this work the statistical variation has been strictly limited to avoid this issue. Whilst the Pb nuclear data employed was from TENDL-2015, FENDL3.1b data was used for the neutron transport of other elements present in the reactor model. A series of simple Bash and Python scripts were used to select different Pb TENDL-2015 ACE files for different runs, before creating and submitting jobs to the local cluster.

Python scripts were used to plot TBR convergence as a function of simulation count (see figure 2.5) and the distributions of simulated TBR (see figure 2.7).

2.3 Input nuclear data

It is instructive to inspect the nuclear data used as input for this TMC simulation. In an unmoderated fusion neutron spectrum the dominant reaction channels for Pb are neutron multiplication (n,2n) and elastic scattering, at approximately 2 and 3 barns respectively.

Nuclide	Mean, μ [b]	RSD, $\frac{\sigma}{\mu}$	Skewness
Pb206	2.11	8.1%	-0.065
Pb207	2.12	10.7%	-0.868
Pb208	2.17	9.7%	-0.120

Table 2.2 TENDL2015 ‘random’ Pb n,2n neutron multiplicity channel cross-section distribution statistics

Figure 2.2 and Table 2.2 show the distributions of TENDL-2015 cross-sections for (n,2n) at 14MeV. Lower values for $\sigma_{n,2n}$ will reduce the neutron multiplication of the blanket and, other quantities being equal, result in a reduced total neutron flux and therefore a lower TBR.

Nuclide	Mean, μ [b]	RSD, $\frac{\sigma}{\mu}$	Skewness
Pb206	2.84	7.5%	0.663
Pb207	2.80	8.0%	0.548
Pb208	2.81	8.1%	1.185

Table 2.3 TENDL2015 ‘random’ Pb elastic scattering cross-section distribution statistics

The elastic scattering data shown in Figure 2.3 and Table 2.3 are instead positively skewed, with high value tails for each isotope, with the most pronounced tail being ^{208}Pb. A greater elastic scattering cross-section will result in an increased likelihood of downscattering

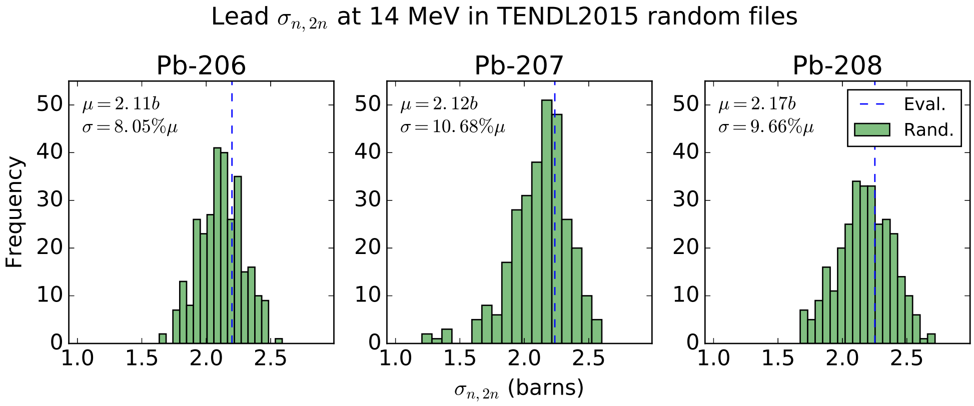

Fig. 2.2 Shown are histograms of $\sigma_{n,2n}$ at 14MeV for the three major Pb isotopes. It can be seen that while ^{206,208}Pb are approximately symmetrical with skewness values close to zero, ^{207}Pb has a skewness of -0.868 indicating a low-value tail. This may or may not be representative of the underlying distribution. The histogram contains all 300 available files for ^{207}Pb, but it could be the case that with more files a Gaussian shape would be recovered.

neutrons to lower energies. The softer spectrum will increase triton production in ^{6}Li as the cross-section increases with decreasing energy, i.e. $\sigma_{n,t}(E) \propto \frac{1}{E}$. However, the elastic scattering cross-section is anti-correlated with the n,2n cross-section in the TENDL data (see figure 2.4). In other words, a high scatter cross-section is typically coupled with a low multiplicity cross-section. This compensating effect decreases the overall uncertainty where individual perturbations on a single channel would result in an unrealistic, larger uncertainty. This inclusion of cross-channel correlation is one of the key advantages of TMC over more traditional uncertainty propagation (UP) methods.

2.4 Results & discussion

The TMC simulation was run for a total of 1559 MCNP simulations, each 84 core-minutes across 32 cores. The total wall-clock time was 3 days, 15 hours.

The mean TBR value is 1.0193 whilst the median is 1.0200, with a one sigma standard deviation of 0.012 or 1.2% of the mean. The TBR distribution is approximately normal, with a small skewness of -0.199, meaning the low-value TBR tail is longer than the high-value tail. Figure 2.6 shows the expected correlation between the n,2n cross-sections used in a given simulation and the TBR attained in that simulation.

Uncertainty propagation in Monte-Carlo type radiation transport problems has often previously been computed using linear perturbation theory approaches. Unfortunately these are only applicable for small changes in the input data. They are also unable to reproduce

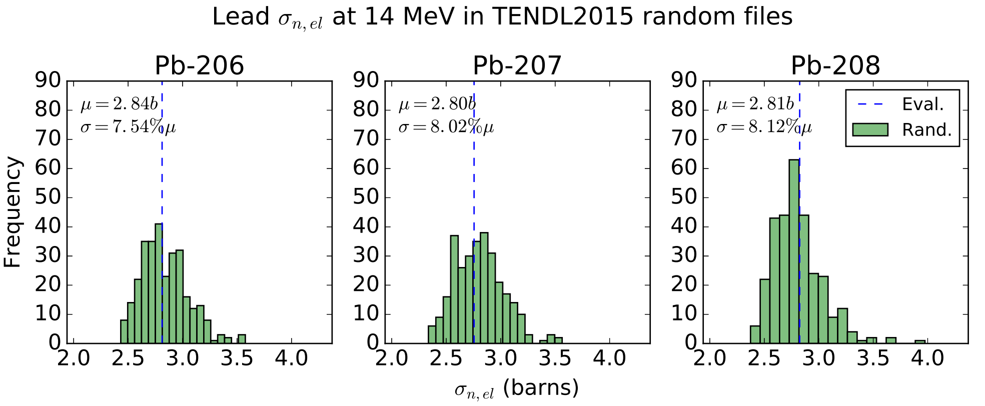

Fig. 2.3 The elastic scattering cross-sections for lead at 14MeV are all positively skewed, with ^{208}Pb having a skewness value of 1.185.

probability distributions of the integral quantity of interest [12]. Whilst figure 2.7 shows a TBR distribution that is not tremendously skewed, that is not to say other fusion quantities will not be. Koning & Rochman have demonstrated that fast and accelerator driven fission systems can have significantly skewed k_{eff} values, best described by an Extreme Value Fit (EVD) [7].

2.5 Conclusion

TBR uncertainty has been computed with the TMC technique, investigating the contribution of uncertain nuclear data from the three major lead isotopes. The standard deviation is 1.2% of the mean TBR. However, note that 5.8% of the distribution is less than unity. While the average value may appear to be feasible, it should be stressed that there is a non-negligible probability of a value below a required limit. The TBR values are relatively low as this particular model has not been optimised for TBR and any practical design should have a TBR $\approx$ 1.1 [4], but in future design studies engineers should be aware of the probability of non-compliant operational parameters.

The TENDL-2015 nuclear data investigated in section 2.3, which is not necessarily Gaussian in shape, has yielded a TBR distribution with a small but finite negative skewness, an extended low-value tail. It is not possible to deduce this shape with more simplified approaches to uncertainty propagation such as linear perturbation theory.

Future work on TBR in HCLL could include the effect of other nuclides and elements which TBR is sensitive to including iron, as well as a completely correlated uncertainty propagation method employing lithium.

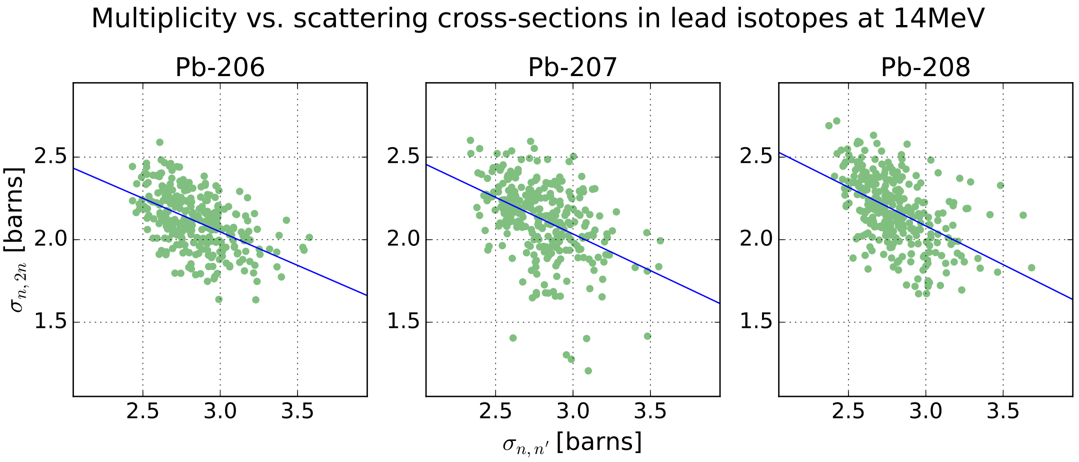

Fig. 2.4 Shown here are scatter plots of the relationship between the scattering and n,2n cross-sections in the TENDL data. The two channels are clearly anti-correlated. A least squares fit has been applied and the resulting linear relationship plotted.

More generally, when solving for integral quantities in nuclear fusion systems, thought should be given to fully-correlated uncertainty propagation and the form of the resulting probability distributions. In particular, whether a non-normal distribution with increased likelihood of extreme behaviour would have engineering design or safety implications for TBR, nuclear heating, fast flux, gas production or damage terms. Moreover, in all analyses for design applications the non-negligible probability of operational parameters in unacceptable regimes should be borne in mind.

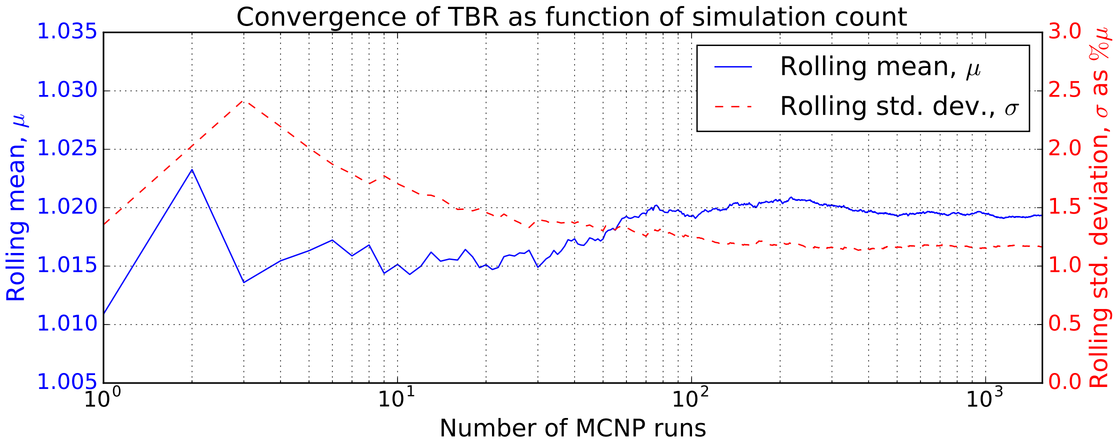

Fig. 2.5 The mean and standard deviation of the TBR distribution is presented as a function of the number of simulations. The TMC simulation can be seen to converge at approximately 400 MCNP runs. $\mu(400) \approx 1.02$ and $\sigma(400) \approx 1.14$.

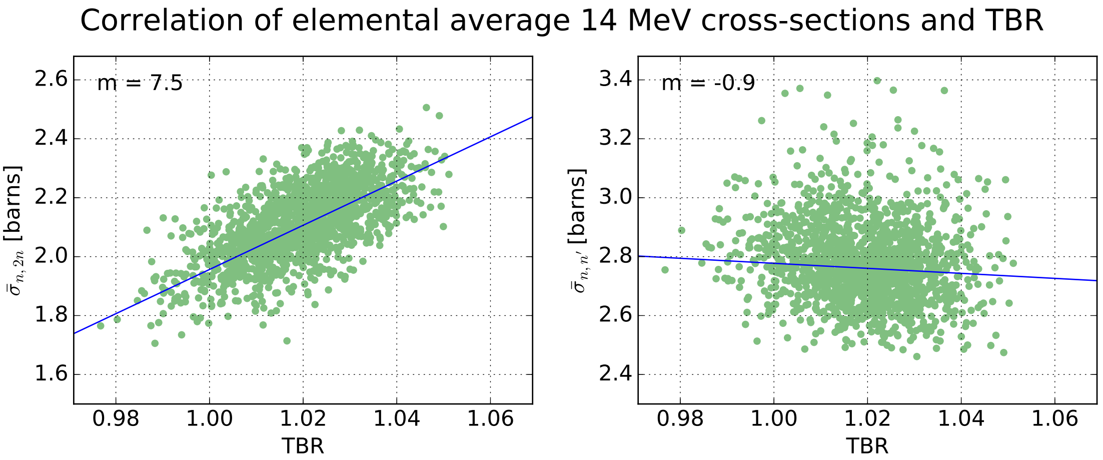

Fig. 2.6 Above are scatter plots of average cross-sections for the n,2n (left) and elastic (right) channels against resulting TBR value. As the cross-sections for each of the three lead isotopes were varied in every simulation, so the cross-sections plotted here are the elemental average values denoted as $\bar{\sigma}_{n,2n}$ or $\bar{\sigma}_{n,n'}$, i.e. all three varied Pb isotopes contribute, weighted by their relative natural abundances. The n,2n cross-section is positively correlated with the TBR value as expected. There is less of a relationship between scattering and TBR.

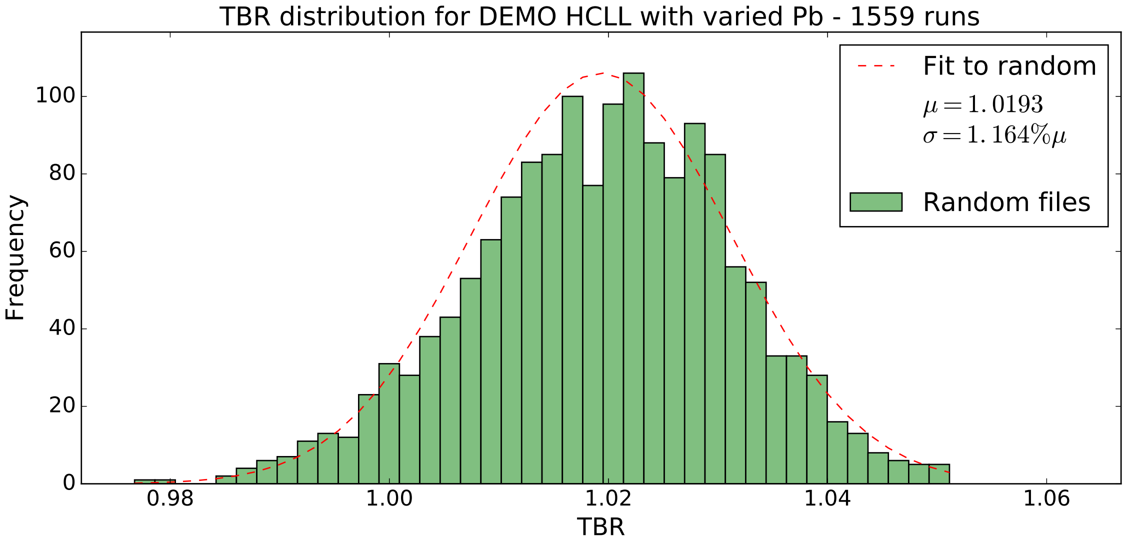

Fig. 2.7 Histogram of TBR values computed with the TMC methodology.

Chapter 3

Quantifying received dose errors introduced by spatial homogenisation of reinforced concrete shielding

3.1 Introduction

An investigation into the process of spatial homogenisation of radiation transport geometry has been performed for reinforced concrete shielding. Using parameters relevant for the ITER fusion experiment, shielding and activation simulations have quantified the effect of homogenisation. The dose received by a person beyond the shield during plasma operation is underestimated by homogenisation. For walls over a meter in thickness it can be by 20%. The shut down dose to a worker on the tokamak side of an activated wall *due to the wall* is overestimated by homogenisation, by a factor of up to 60.

In nuclear engineering, quantifying the absorbed dose to radiation sensitive components, or the equivalent dose to personnel usually requires crafting a computer model of the problem, making a series of assumptions and simplifications in the process. For reinforced concrete radiation shields, this often entails either homogenising the reinforcing bar (abrev. rebar) with the concrete, or even neglecting the presence of rebar entirely. However, steel has a high density $\sim 7.8 g \cdot cm^{-3}$ and a markedly different elemental composition to low density $\sim 2.2 g \cdot cm^{-3}$ concrete. Steel is an alloy of many different elements but principally high-Z Fe. Whereas concrete largely consists of low-Z elements, O, Si & H (in descending atomic density order).

The process of homogenisation introduces systematic error into the reported solution of any radiation transport problem by moving steel and adjusting the density.

The discrepancy in results between heterogeneous and homogeneous modelling approaches is investigated in this work. Querying the strength of correlation of the discrepancy with a given parameter requires producing radiation transport geometry in pairs, as shown in figure 3.1.

The heterogeneous wall is constructed of a large concrete block, with two meshes of rebar, one buried below each face. The distance from wall exterior to rebar is known as the cover depth. Connecting the two meshes are a small number ($4m^{-2}$) of narrow gauge stirrup bars.

Material compositions, wall widths, rebar arrangements and steel fractions have been determined from ITER drawings and specifications for concrete walls in the tokamak building. The results should give a good idea of the implications of the homogeneous modelling approximation at ITER. The work was also conducted with a moderated ITER DT fusion neutron source spectrum. As such, this investigation should not only be instructive concerning ITER shielding, but also other DT fusion facilities.

3.2 Method

The principal modelling simplification under investigation is that of spatial homogenisation. As such, for each set of independent and dependent variables, at least two simulations will be performed. One will have a high-fidelity model of the real-world problem geometry with rebar and stirrups faithfully reproduced. The other will smear the rebar across the concrete, homogenising the two materials into one with a density equal to the mass weighted sum of the concrete and steel constituents.

The implications of homogenisation prove to be different for on-load and shut-down (activated) dose rates. It is helpful to consider them seperately.

3.2.1 Prompt neutron & gamma radiation

Determining the dose to personnel beyond a wall requires knowledge of the radiation fluxes there. The on-load gamma flux $\phi_\gamma(x,y,z,E,t)$ and neutron flux, $\phi_n(x,y,z,E)$, can be computed with Monte Carlo techniques, spawning neutrons from a prerecorded source distribution, $P(x,y,z,E,\Omega)$ at a particular point with a given energy and angle. These particles may propagate through the wall, scattering, being absorbed, exciting nuclei (which later relax through radiative emission) and perhaps leaking out of the back of the shield wall. Tallying this leakage flux of neutrons and photons is the main task of calculating a dose due to radiation.

Radiation transport was conducted with MCNP6v1.0. The nuclear data employed was the continuous energy Joint Evaluated Fission and Fusion file 3.2 (JEFF3.2) for neutron transport and MCPLIB84 for photon transport. Input decks for MCNP were produced with a bespoke Python program written by the author, this automated approach allowed for easy parametric study.

The MCNP relative error, $R = \frac{\sigma_s}{\mu_s}$ which is the ratio of sample standard deviation to sample mean was kept to below 0.1 for all energy bins and mesh voxels.

The source spectrum plotted as figure 3.2 has the recognisable DT peak, but has been significantly thermalised. The apparent absence of a Maxwellian shape around the facility temperature is because of the coarse energy binning used for this tally.

The effective dose to humans is a function of the energy and type of radiation. It takes into account the varying susceptibilities of different tissues in the human body. For radiation protection, this is the typical figure quoted when specifying a dose rate. Translation from fluence or flux is by a table similar to that plotted as figure 3.3.

3.2.2 Delayed gamma radiation

The calculation of $\phi_\gamma(x,y,z,E,t)$ where t is some time after cessation of plasma operation comprises three main steps:

1. 1) Neutron transport—as previously, compute the neutron flux during plasma operation, $\phi_n(x,y,z,E)$, recording the neutron flux binned by energy over a spatial mesh.
2. 2) Activation—determine the appropriate irradiation scenario, then activate and transmutate the materials present in the problem geometry.
3. 3) Photon transport—using the distributed decay gamma source produced by step 2), conduct a radiation transport run to determine the photon flux, $\phi_\gamma(x,y,z,E,t)$, converting to effective dose as required.

As for before, radiation transport was conducted with MCNP6 v1.0. Activation was conducted with the FISPACT-II code and EAF2010 nuclear data.

The irradiation scenario employed for the activation step was ITER's SA-2, which gives a good representation of the ITER experimental programme total fluence and of the final, end-of-life pulses.

Homogenising reinforced concrete

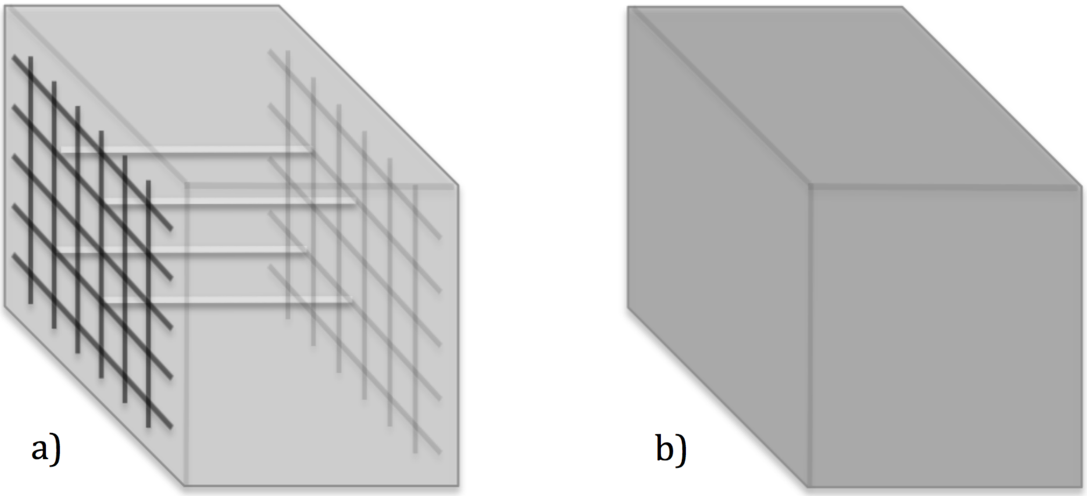

Fig. 3.1 The two modelling approaches considered in this investigation. a) Heterogeneous, where the steel reinforcing bar and stirrups are explicitly modelled. b) Homogeneous, where the mass of rebar is ’smeared’ through the concrete. The new homogenised material has a greater density than plain concrete, conserving mass.

Neutron source spectrum

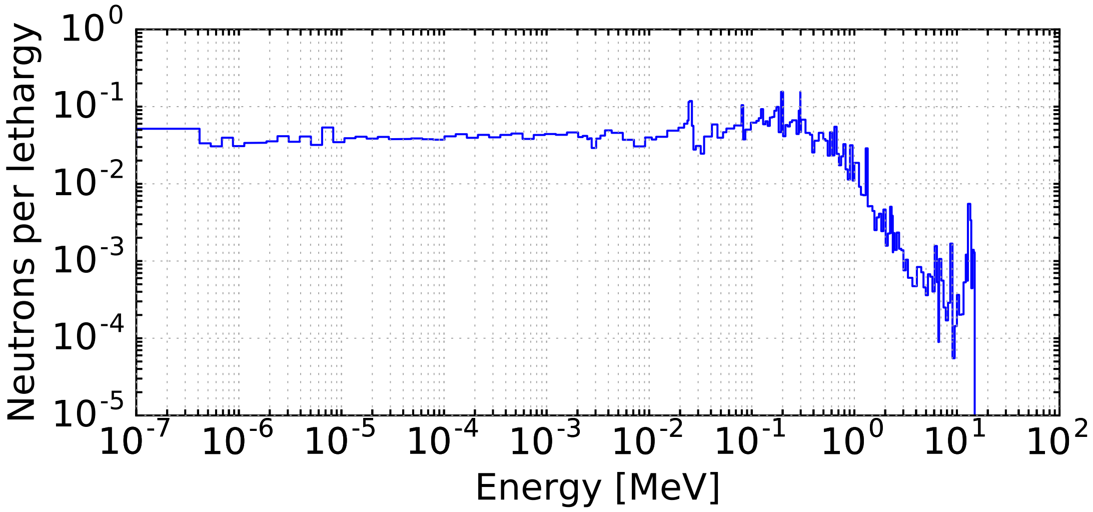

Fig. 3.2 Neutron spectra for incident radiation. This spectra was recorded in 175 energy groups from the back of the ITER Neutral Beam assembly, immediately inside the bioshield concrete wall.

3.3 Results & discussion

3.3.1 Transmission of prompt radiation

The leakage neutron spectra for a thick (2.1m) concrete wall is shown below as figure 3.4. The flux has been severely reduced by its interaction with the wall, decreasing from the source by an order of magnitude each 20cm traversed.

The reduced thermal flux in the homogeneous case is in part because steel is now available for neutron interactions throughout the depth of the wall. Steel has a greater combined capture cross-section than concrete (radiative capture shown in figure 3.5), this acts as a neutron sink.

Plotting the ration of the leakage neutron spectra as figure 3.6 we can see the differences more easily. Thermal flux is underestimated by more than a factor 2. But also, fast flux in the 1keV–1MeV range is underestimated by ~ 1.2. The fast flux discrepancy is correlated with wall thickness and is negligible for thin (<1m) walls.

Figure 3.7 shows how the discrepancy due to the homogeneous approximation varies with wall thickness. It can be seen that the effect is greatest for neutrons. It also plateaus at $\sim 1m$ wall thickness.

3.3.2 Shut Down Dose Rate

After operation of a tokamak, repairs and maintenance are often necessary. This section explores the shut-down dose due to be received from the wall itself. It assumes a worker is inside the bioshield at ITER, stood 30cm from the inner surface of an activated wall.

Spatial homogenisation acts to overestimate the SDDR beyond 1 day (see figure 3.8). The homogenised steel in the first few centimeters of the wall is activated by a stronger neutron flux than the physical rebar, located some 5–10cm inside the concrete (the cover depth).

The mean free path of neutrons near the surface is $\sim 2cm$ (see figure 3.9) and as such a typical neutron will undergo several collisions before arriving at the rebar in a heterogeneous simulation. However, in a homogeneous simulation a small amount of steel is present right at the very surface of the concrete, as it is present throughout the simulation. This steel is exposed to an intense neutron flux and is activated accordingly.

The plot shown as figure 3.10 is produced with data from the activation solver FISPACT-II. Shown are estimates for a contact dose with concrete and steel. As the steel is buried within concrete, the numbers plotted here are not a substitute for transporting decay γ photons from their birth to their death. However, they do give a good feel for which nuclides are responsible for the activity of a material at a given time. It is clear that after ^{28}Al and ^{24}Na decay in concrete, it has become substantially less active. It is around this time that steel becomes

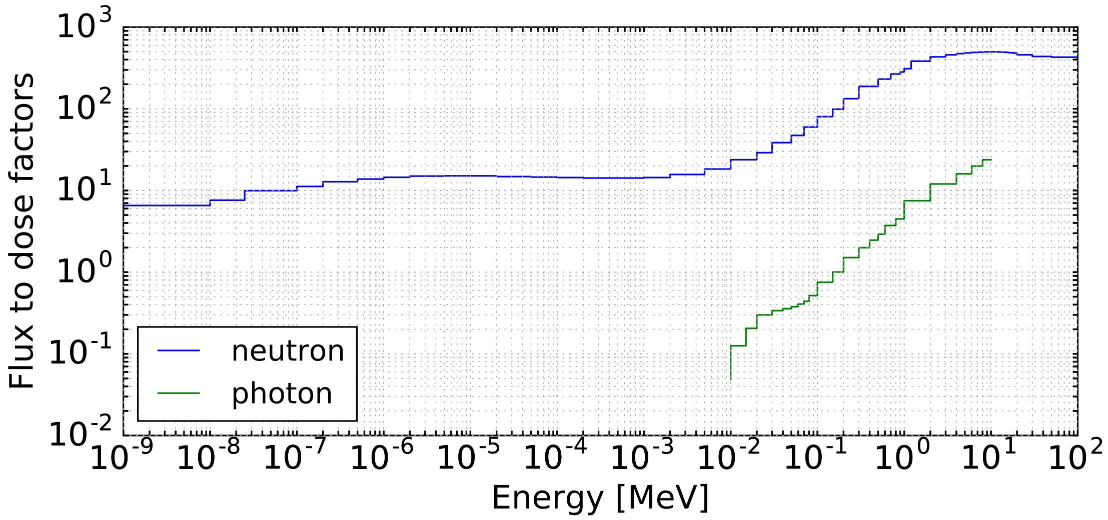
ICRP74 flux to dose factors

Fig. 3.3 The flux to dose conversion factors for neutron and photon exposure.

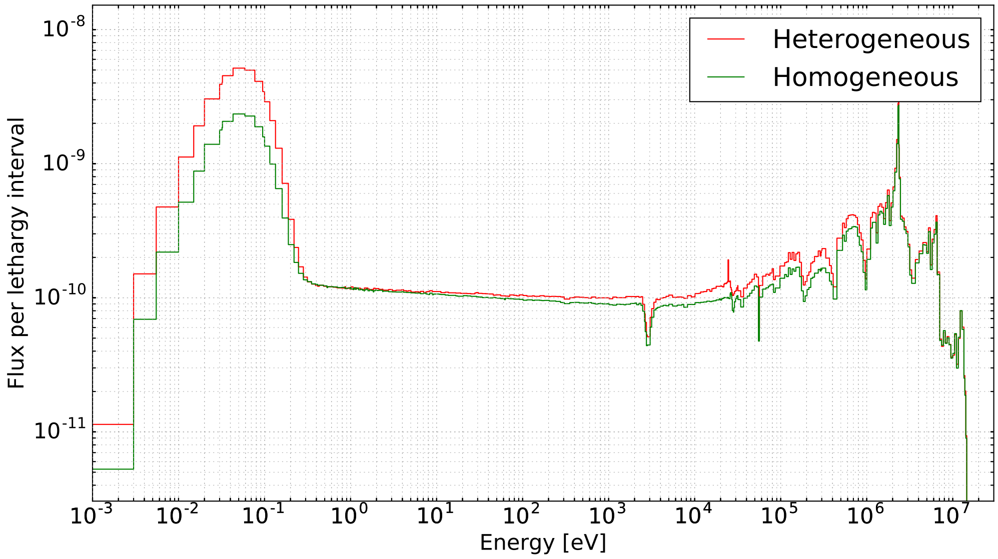
Transmitted neutron spectra

Fig. 3.4 The neutron spectra leaving the shield for the heterogeneous and homogeneously modelled cases. Note the substantially reduced thermal flux in the homogeneous simulation. This spectrum has been binned with a finer energy grid than the source, the TRIPOLI 315 group structure.

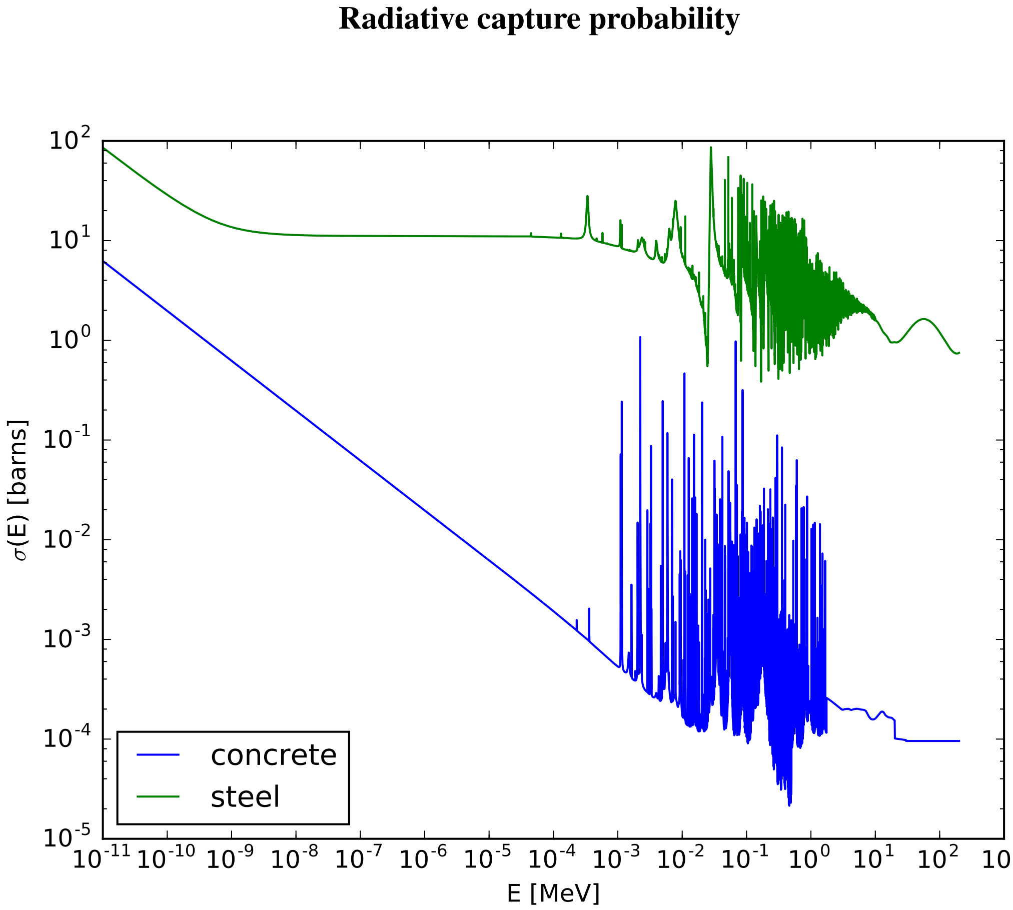

Fig. 3.5 The nuclear properties of steel and concrete are substantially different. Shown here is the cross-section for (n, γ) in both materials.

the dominant contributor to dose and the homogeneous modelling approach diverges from heterogeneous.

3.4 Conclusion

The spatial homogenisation modelling approximation for reinforced concrete underestimates the dose due to neutrons by up to 20%. The dose due to on-load photons can be underestimated by up to 8%.

The SDDR is instead overestimated by homogenisation, by up to a factor 60 at times beyond a day.

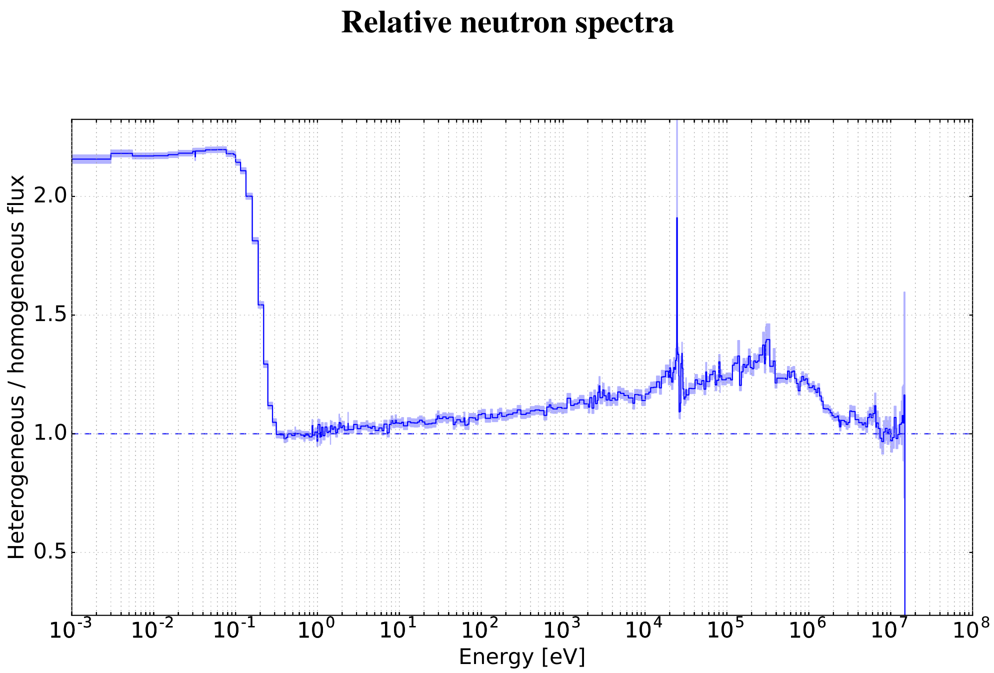

Fig. 3.6 The homogeneous flux increases are readily visible here.

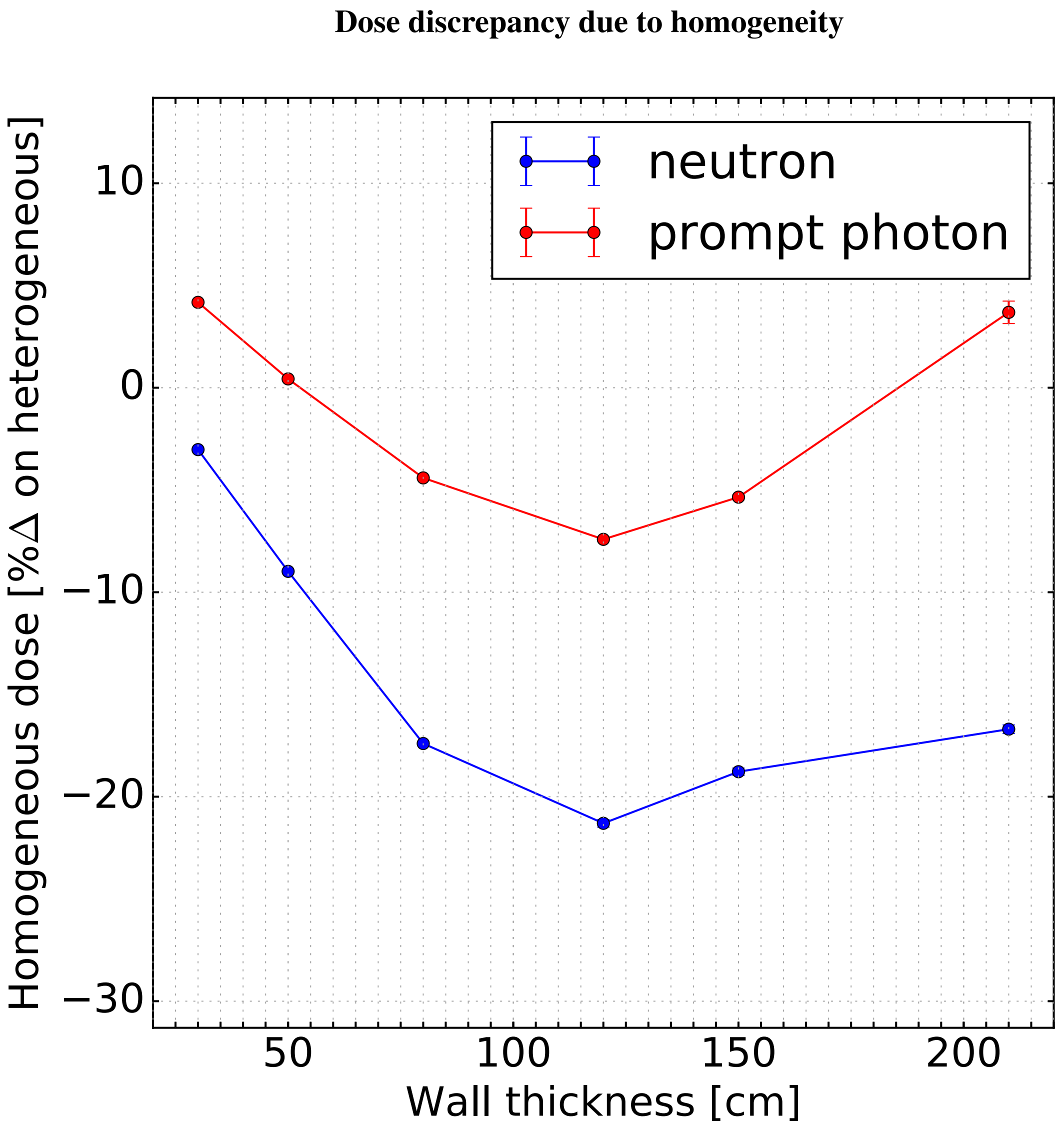

Fig. 3.7 The discrepancy between modelling approaches is a function of the wall thickness for thin walls.

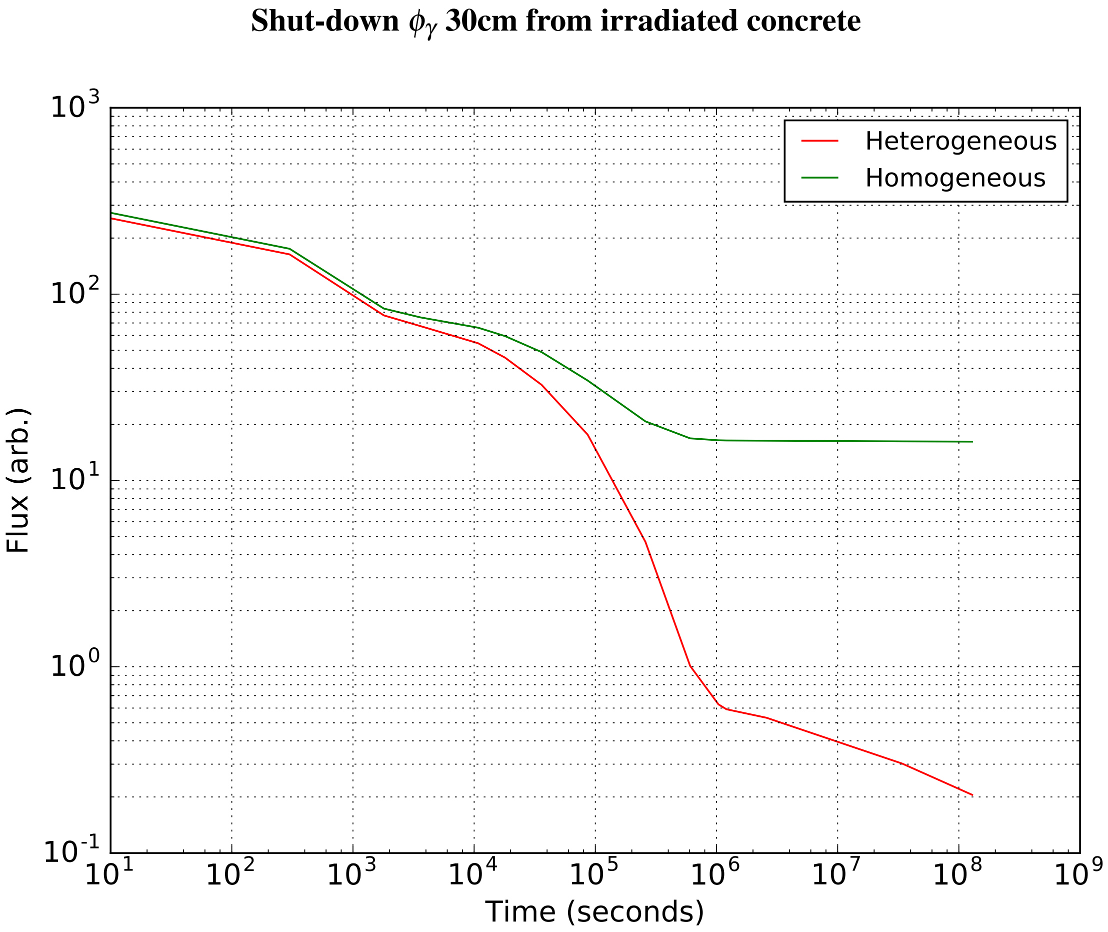

Fig. 3.8 The total ϕ_γ as a function of cooling time. The homogeneous simulation gives a significantly increased value at time steps beyond $10^5 s$ or approximately 1 day.

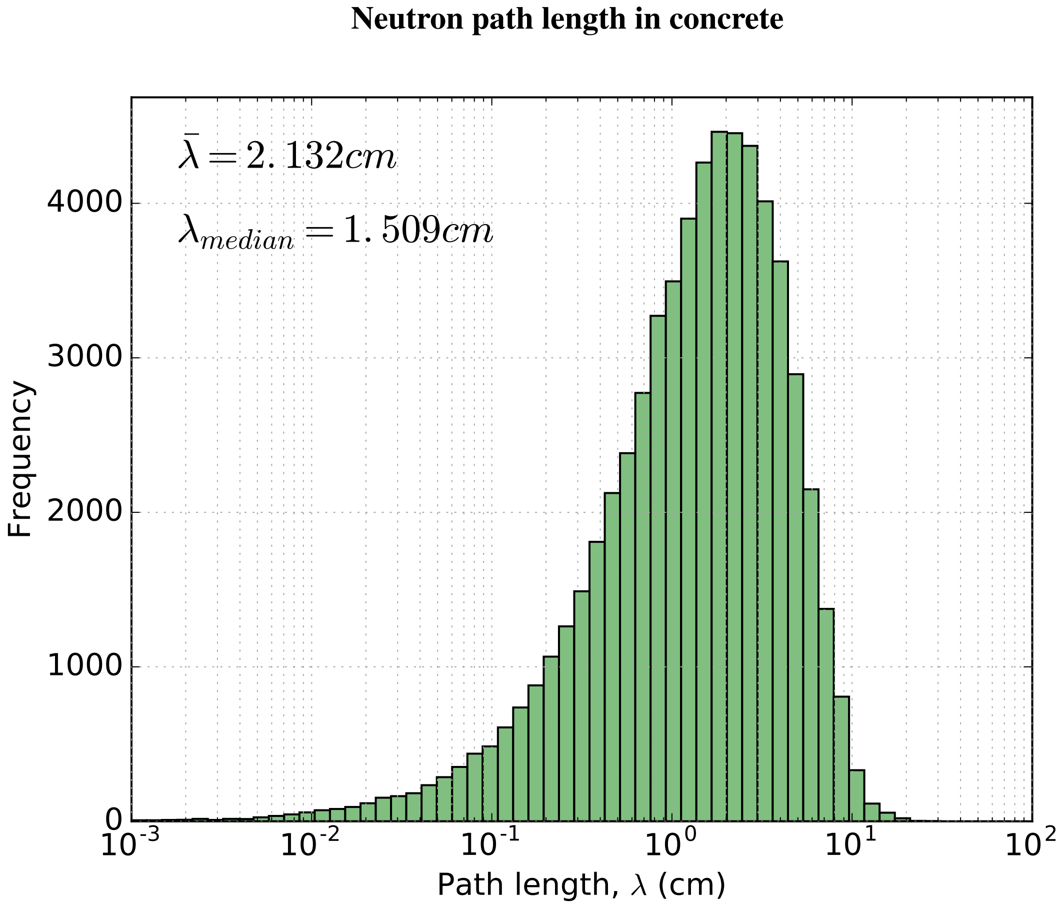

Fig. 3.9 The path lengths of neutrons in pure concrete are shown as a histogram. There is a wide distribution with a mean of approximately 2cm.

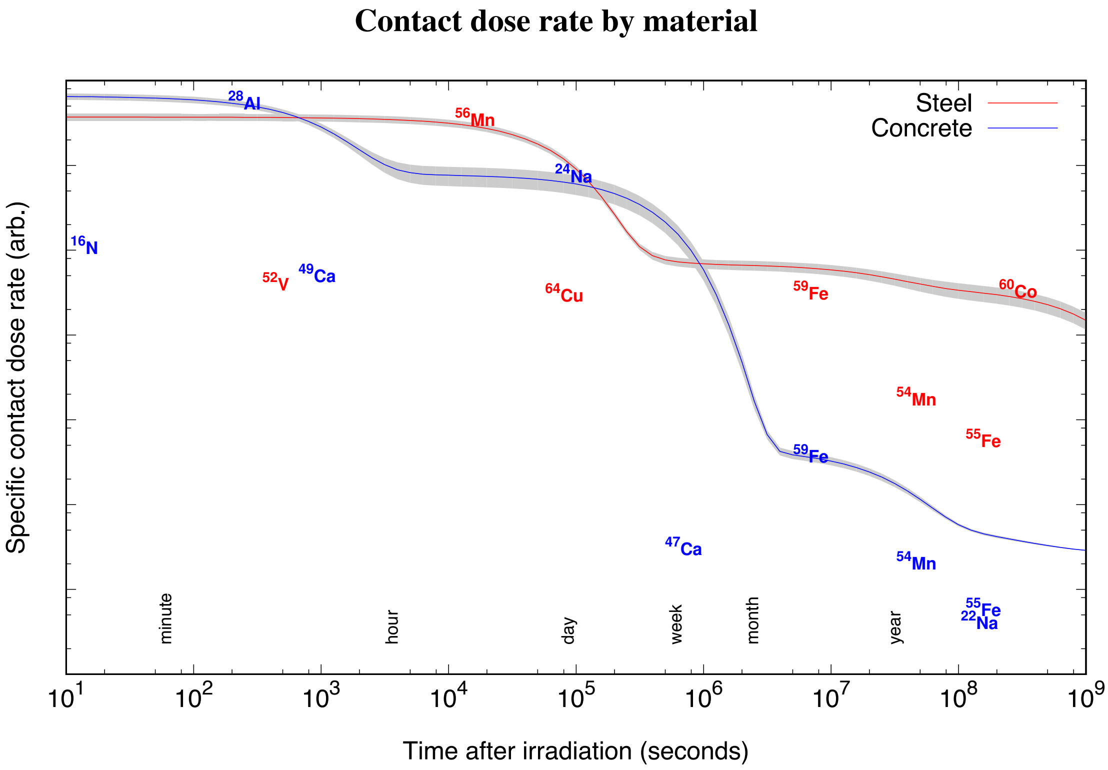

Fig. 3.10 This plot shows an estimate for the specific contact dose rate due to steel and concrete irradiated under the ITER SA-2 scenario. Nuclides which contribute a significant fraction of the dose are shown with their abscissa value as their half-life, $t_{\frac{1}{2}}$.

Chapter 4

Optimising energy group structures for neutron activation calculations in fusion systems

4.1 Outline

This study utilises self-shielding factors as a means to optimise energy group structures for fusion activation calculations. Informed by an analysis of important fusion resonances and a survey of relevant incident particle spectra, we develop and test two new group structures designed to more accurately represent the physics of nuclear reactions. They are compared to group structures commonly used in fusion research & analysis. When used in a JET activation foil scenario, the optimised group structures outperform reference group structures, such as CCFE-709, while requiring fewer bins.

4.2 Introduction

Nuclear simulations for fusion devices are essential to determine material damage, activation-transmutation and to perform dose rate analyses. While continuous energy Monte Carlo modeling can be used to directly calculate reaction rates, due to the very large number (potentially tens of thousands) of possible reaction channels, it is impractical to compute all nuclear reactions of interest by this so-called point-wise approach. A separate inventory code, such as FISPACT-II [16], utilising a discretised incident particle spectrum is typically used to calculate all of these reaction rates, solve for the time-dependent nuclide inventory and provide various responses and source terms. This multi-group method is computationally efficient, but introduces self-shielding errors.

The likelihood of interaction between an incident particle and a nucleus is a highly non-linear function of energy in the resonant energy region. The cross-section, $\sigma(\mathrm{E})$ and the associated reaction rate, RR(E), may vary by several orders of magnitude within a few electron-volts. The number of bins that the energy domain is discretised over has a strong influence on the accuracy of the result. While increasing the number of bins increases the accuracy it also increases the time required to converge an input spectrum and the memory required to record this information[1]. In addition to the number of bins, their bound locations have a strong relationship to the result accuracy. The integer bin count number and bound locations energy vector are together known as an energy group structure. This paper presents results from a novel method for optimising energy group structures given a selection of materials and a guessed spectrum.

There have been several previous efforts to optimise neutron energy group structures. Certain applications lend themselves to highly targeted group structures. For example, fission reactor lattice physics calculations are typically interested in determining a few reaction rates to very high accuracy. The Studsvik team who develop the CASMO-5 lattice physics code employ a neutron group structure with very fine resolution around the principal ^{238}U and ^{240}Pu resonances [11]. Covering these areas with a fine energy grid results in a more accurate estimate of key reaction rates and hence calculation of the neutrons absorbed and consequently lost from the system. Particle Swarm Optimisation (PSO) has been used multiple times to improve bin bound placement for multi-group libraries used for reactor physics applications [17][2][1][5]. Morgan et al. [10] have explored hyperfine multi-group (MG) data as an alternative to the interpolation of point-wise (PW) data as typically employed by particle transport codes such as MCNP6.1 [6]. Some attention has been directed towards the refinement of reaction rate calculation for specific elements and nuclides in fusion scenarios. For instance, work on the spatial heterogeneity of tungsten transmutation has been undertaken by **?**] who used the CCFE 709 bin group structure and careful application of self-shielding factors to accurately determine reaction rates.

As indicated above, a resonant material of particular interest to fusion plant designers is tungsten, with $^{186}\mathrm{W}(n,\gamma)$ shown in figure **??**. This figure highlights the difficulties of determining reaction rates to a high accuracy. ^{186}W has a large resonance at 18 eV and the energy-integrated reaction rate within this resonance typically dominates the total reaction rate. With the coarse group structure shown in the figure, an unshielded approach to computing the reaction rate yields values several times the ‘true’ point-wise value.

---

[1] A concern for simulations with millions of voxels, common in activation-dose calculations.

The self-shielding of resonant materials other than tungsten has yet to receive much attention in nuclear analyses of fusion power systems. A robust approach for accurately determining reaction rates for any material composition would be a welcome tool for future analyses. The rest of this paper details the first results of one approach, namely the intelligent discretisation of spectra and nuclear data, applied to an activation foil problem.

4.3 Method

The radiation transport geometry utilised in this study is the JET tokamak located near Abingdon, Oxfordshire. Octant 8 of the tokamak has previously housed the Long Term Irradiation Station (LTIS) for exposing activation foils to the JET neutron field. A variety of (n,γ) effective cross-sections have been calculated in various materials and for a selection of energy group structures. Some of these group structures are optimised for the materials present in the simulation, while others are standard group structures in common usage today.

The calculation of effective cross-sections were carried out using three different techniques:

1. Multi-group FISPACT-II unshielded collapse
2. Multi-group FISPACT-II shielded collapse
3. Point-wise MCNP6 Monte Carlo Estimator (MCE)

Methods 1 & 2 discretise the incident spectrum, over a $\phi(E)$ and $\sigma(E)$, taking the inner product of two vectors of constants,

$$\vec{\phi}\cdot\vec{\sigma} = \sum_i \phi(E_i,E_{i+1})\sigma(E_i,E_{i+1}),$$

as the sectrum-averaged, effective cross section. However, for each group interval, $(E_i,E_{i+1}]$ the true functions $\phi(E),\ \sigma(E)$ are not contant. Regions with resonances in the cross section cause local decreases in the neutron flux, resulting in significant 'self-shielding' errors with the multi-group method. To address this, self-shielding factors, SSF(E_i), may be used to account for these resonance effects.

An incident spectrum, material inventory and nuclear data are input to FISPACT-II. The spectrum and interaction nuclear data are then collapsed to generate one-group effective cross-sections. With the addition of probability table data generated with CALENDF-2010 [15], SSF(E_i) are calculated for both the resolved and unresolved resonance regions.

Method 3 employs nuclear cross-section data with tens of thousands of points per reaction channel, interpolating between them to approximate a continuous energy treatment. The effective radiative capture cross-section can be determined from the point-wise calculated (n,γ) reaction rate as equation 4.1.

$$\sigma_{\text{eff}} = \frac{\int RR_{n,\gamma}(E)dE}{\int \phi(E)dE} \tag{4.1}$$

4.3.1 Reactions

The effective cross-sections calculated for this study were a series of radiative capture reactions in metals. These reactions often have a large fraction of their total reaction rate within the neutron slowing down region between thermal and fast energies. Hence, an accurate resonance treatment is required for accurate results.

Reaction	$E_{\text{first res.}}$ (eV)	E_{URR} (eV)
$^{95}\text{Mo}(n,\gamma)^{96}\text{Mo}$	4.47E1	5.87E4
$^{181}\text{Ta}(n,\gamma)^{182}\text{Ta}$	4.27E0	4.00E3
$^{182}\text{W}(n,\gamma)^{183}\text{W}$	4.16E0	9.91E4
$^{186}\text{W}(n,\gamma)^{187}\text{W}$	1.88E1	1.21E5

Table 4.1 Shown above are the reactions simulated in this study. $E_{\text{first res.}}$ indicates the energy of the first resonant peak in the interaction cross-section. E_{URR} defines the end of the resolved resonance range (RRR) and the start of the unresolved resonance range (URR) where experimental energy resolution is insufficient to resolve individual resonances.

The reaction channels chosen for study are listed in table **??**. The nuclides listed are found in the designs of fusion power systems; iron is the principal constituent of all steels, cobalt a steel impurity which dominates shut down dose rates at intermediate time scales, molybdenum an important steel alloying element, tantalum is being investigated for use in high-heat flux componentry and tungsten is a current first choice for a plasma facing high-heat flux material.

4.3.2 Group structure optimisation

This study tests various group structures against a point-wise reference. We have generated two of the test group structures, attempting to optimise them to accurately calculate reaction rates for a set of nuclides.

To assemble a distribution for bin density we define several piecewise functions for identifying where, in the energy domain, self-shielding factor modifications are important and to indicate where resolution should be concentrated.

Equation 4.2 describes the cumulative differences between reaction rates for some energy group, $E = (E_0, E_1, \ldots, E_N)$.

$$S(E_g) = \sum_{i=0}^{g} \mathrm{RR}(E_i) - \mathrm{RR}(E_i)\mathrm{SSF}(E_i) \tag{4.2}$$

The cumulative, effective self-shielding distribution,

$$C(E_g) = 1 - \left(\left(1 - \overline{\mathrm{SSF}}\right) \frac{S(E_g)}{S(E_N)} \right) \tag{4.3}$$

begins at 1 for the first energy group, and to reduce to a minimum of the effective self-shielding factor $\overline{\mathrm{SSF}}$,

$$\overline{\mathrm{SSF}} = \frac{\sum_{g=0}^{N} \mathrm{RR}(E_g)\mathrm{SSF}(E_g)}{\sum_{g=0}^{N} \mathrm{RR}(E_g)}. \tag{4.4}$$

This function, $C(E)$, gives a dimensionless measure of the importance of self-shielding modifications to interaction data. It allows comparison between nuclides of different cross-section values, as it is scaled between unity and the nuclide's $\overline{\mathrm{SSF}}$. Discontinuities in C(E) show regions with large effective self-shielding. An example of a cumulative SSF distribution is shown in figure **??**.

The differences between discrete elements of the cumulative distribution provide an effective self-shielding distribution,

$$D(E_g) = C(E_g) - C(E_{g-1}), \tag{4.5}$$

that identifies the relative contributions from each bin to the overall self-shielding effect. It is shown as the effective self-shielding distribution in figure **??**.

As such, $D(E)$ indicates where the the group structure requires enhanced resolution in an improved group structure. However, outside the resonance ranges, for example for E $< 10^{-2}$ or E $> 10^5$ eV, this distribution is identically zero. To enforce a minimum bin density, a constant, b, is added to all bins of $D(E)$ in the algorithm employed.

$$b = \frac{D(E)\Delta E(E)}{\frac{n_{bins}}{bpd_{min}} - d} \tag{4.6}$$

The minimum bins per decade, bpd_{min} must be specified. Where d is the number of decades described by the group structure, n_{bins} is the total number of bins required of the new group structure and $\Delta E(E)$ is an array of the input group bin widths.

$$\rho(E) = D(E) + b \tag{4.7}$$

$\rho(E)$ is an array of proposed local bin densities, on the input group structure. This is then rebinned into equal areas as per equation 4.8 to determine the new, optimised group structure.

$$\int_{g=i-1}^{g=i} \rho(E_g)dE = \frac{1}{n_{\text{bins}}} \int_{g=0}^{g=N} \rho(E_g)dE \tag{4.8}$$

The group structures tested in this study are listed in table **??**. The two groups, 280 and 650, generated by our process were optimised for all stable nuclides of the following elements: Fe, W, Mo, Nd, Sn, Zr, Cu, Co and Ta. This means we performed the nuclide-wise integral of $\rho(E)$ for all naturally occurring isotopes of these elements.

n_{bins}	E_{min} (eV)	E_{max} (eV)	bpd_{res}	Description
709	1E-5	1E9	50	CCFE
650	1E-5	1E8	37–101	Optimised fine
315	1E-5	1.94E7	24–50	TRIPOLI
280	1E-5	1E8	11–73	Optimised coarse
175	1E-5	1.96E7	5–22	VITAMIN-J

Table 4.2 Comparison of group structures tested, noting their bin counts, n_{bins}, the energy range over which they are defined and the bins per decade, bpd_{res} they employ in the resonant region.

4.3.3 Radiation transport

In order to compare the performance of the different group structures, incident particle spectra were obtained. As previously mentioned, the LTIS foil holder is located within Octant 8 of the JET facility. The LTIS MCNP model [9] was integrated into a reference JET model. The LTIS was populated with foils of the materials noted in table **??**. The simulation was set to tally the reaction rates of interest in each of the foils in each specified group structure. Point-wise tallies were also included.

4.4 Results & Discussion

A set of sample LTIS spectra are as shown in figure **??**. These particular spectra are from within the tungsten foil. Resonances both within the tungsten and the surrounding materials have resulted in flux depressions. An expanded view of the ^{186}W 18 eV resonance is shown as figure **??**. The degree to which the resonances are resolved by the different group structures is a function of the bin resolution around the resonance. The 709 group, with a standard 50 bins per decade reaches down into the 18 eV resonance, recording a fluence of 3.5E-9 whilst the optimised group structures, 280 and 650 record 2.32E-9 and 1.26E-9. The standard group structures 175 and 315 which are much coarser in this region record a minimum fluence more than an order of magnitude greater than the 650 group structure.

Figure 4.4 shows a comparison of collapsed cross-sections for ^{182}W. The abscissa lists each group structure tested. A pair of data points exist for each group structure, one with the use of self-shielding factors (shielded) and one without (unshielded). The abscissa order is a sorted such that the unshielded values decrease from left to right. The left ordinate indicates the absolute cross-section value in barns, while the right ordinate gives the cross-section as a percentage change over the point-wise (reference) value, i.e. +100% means the multi-group calculation has over-estimated the cross-section and therefore reaction rate by a factor of 2.

As would be expected, in a simple, unshielded case having more groups and therefore a larger number of groups per energy decade tends to give multi-group results closer to the reference point-wise result. Flux depressions are better resolved with narrower groups and therefore the reaction rate resulting from resonances is not overestimated to the same degree. However, with the exception of ^{181}Ta, the 650 optimised group, and even the 280 optimised group perform better than the 709 group in the unshielded regime. Their narrow groups are targeted where most useful, around the resonances which were poorly described by a equal logarithmically spaced group structure.

With regards to individual groups, the 175 group used unshielded performs very poorly, overestimating the reaction rate by at least a factor of 3 in all cases. The 650 optimised group is always within 50% of the point-wise result and is the best performing group.

As might be expected the shielded results show far less variation between groups. 280, 315, 650 & 709 demonstrate largely similar behaviour when used in conjunction with self-shielding factors. 175 does again over-estimate, between 0% and 120% depending on the nuclide.

The ^{181}Ta (figure 4.6) and ^{95}Mo (figure 4.7) results indicate over-shielding, that is self-shielding factors over compensating for a poor description of the spectrum. This is particularly pronounced for the 315 group in ^{95}Mo, where the shielded result is 40% less than the point-wise result. This is due to the application of one set of self-shielding factors over the entirety of the foil depth. Although only 500 microns, the compound geometric effects are essential and are the subject of further work.

4.5 Conclusions

This study has investigated how an incident spectrum and nuclear data library are discretised in energy (i.e. the group structure) effects the accuracy of reaction rate calculations. The selection of group structures trialled included three in current use and two which were optimised by our own, novel method.

The accuracy of multi-group reaction rate calculations is severely hampered by using the legacy VITAMIN-J 175 group structure. In the context of this activation foil problem, coarse group structures can give reasonable results if used in conjunction with modifying self-shielding factors. If used, self-shielding factors must be applied carefully, with potential geometric shielding effects considered. If used inappropriately, over-shielding may result, which may not be conservative depending on the context.

An optimisation algorithm has been demonstrated. The algorithm can generate and optimised set of bin bounds, given a ‘guess’ spectrum and a target nuclide set. An unshielded multi-group calculation using an optimised group structure with 280 bins has more closely approximated the point-wise result than the 709 unshielded multi-group calculation in the majority of cases examined.

Further work will improve on the optimisation algorithm and explore the performance of optimised group structures in a wider array of circumstances. Iterative application of the algorithm will be investigated as well as geometric self-shielding effects.

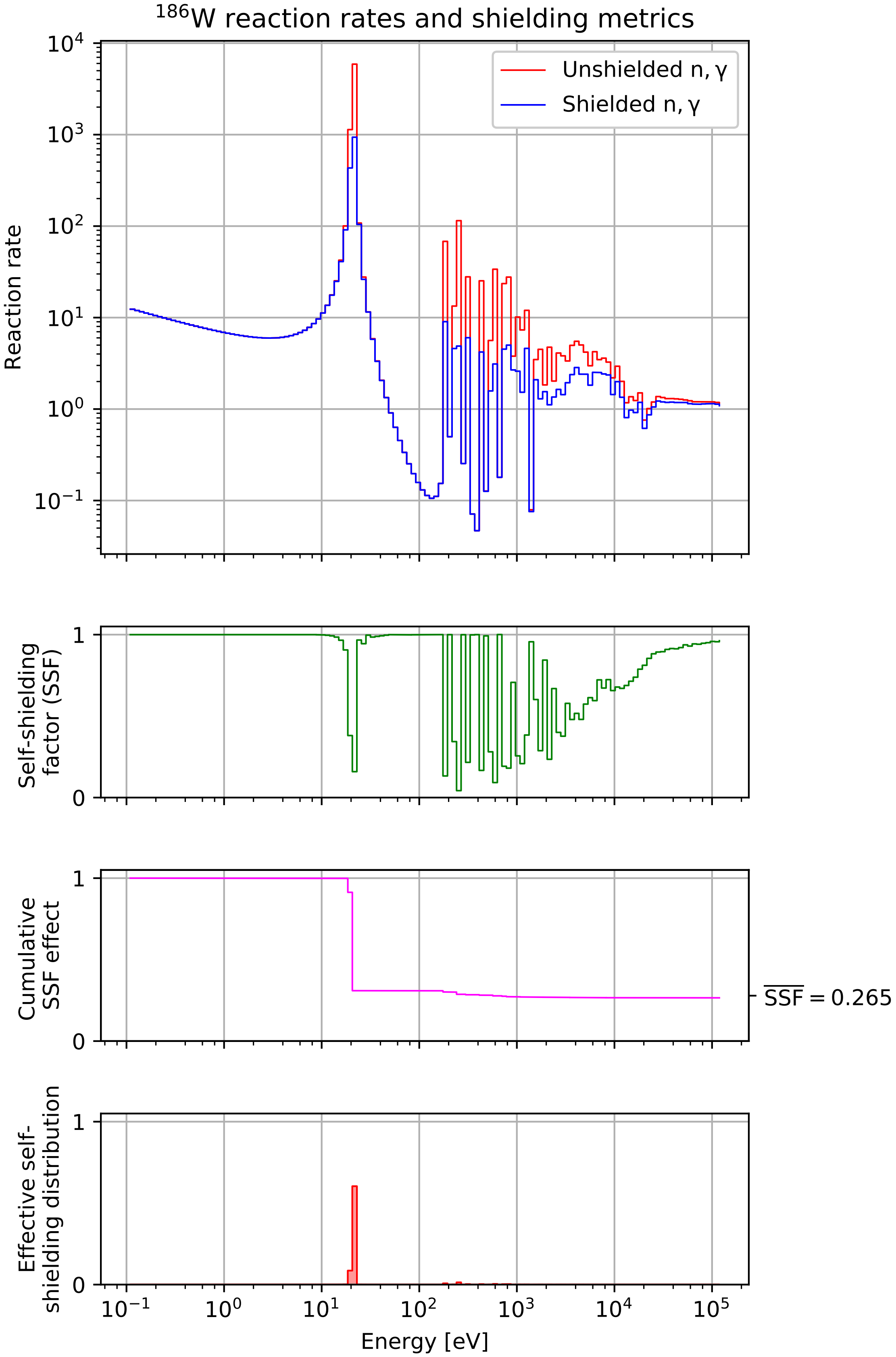

Fig. 4.1 Shown in the upper plot is a ^{186}W radiative capture reaction rate, both unshielded and shielded. The incident particle spectrum in this case is a power function of energy, i.e. $\phi(E) = E^x$ where x is some constant. The second plot shows the calculated self-shielding factors as a function of energy for this reaction, given an elemental material composition. The third and fourth plots are derived quantities used for group structure optimisation. See

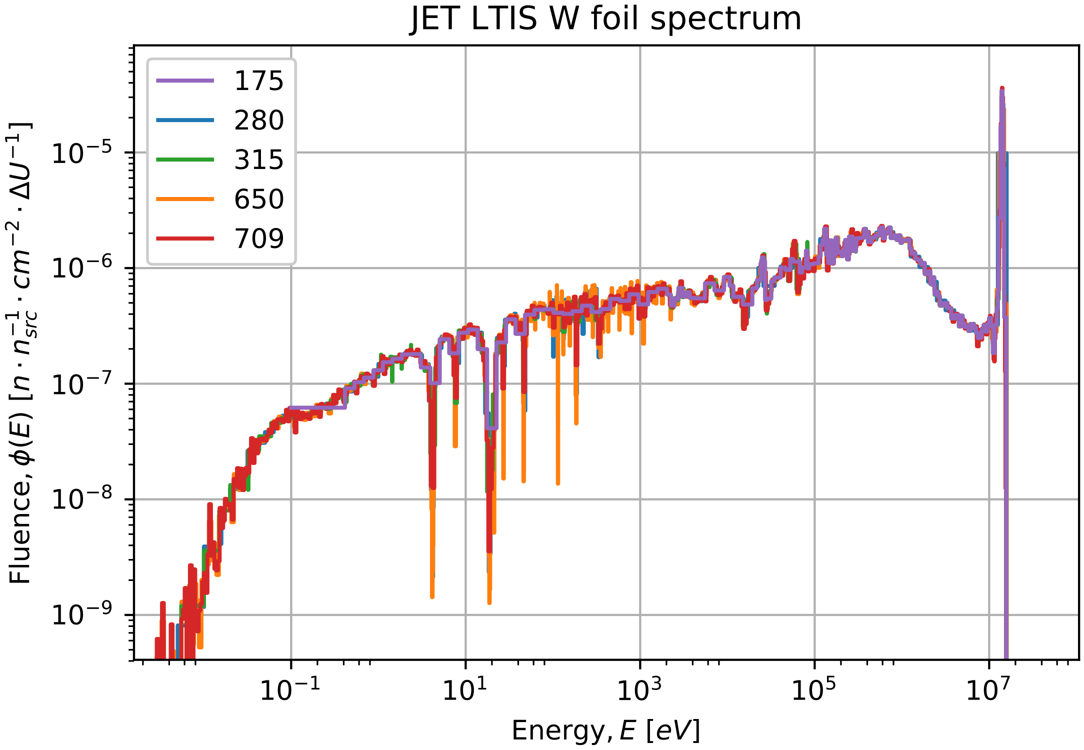

Fig. 4.2 Typical DT neutron spectrum within the LTIS activation foil holder. The fluence of each bin has been divided by the lethargy width for that bin, ΔU. The spectrum is hard, with little thermalisation as a consequence the foil's proximity to the plasma. The same neutrons have been binned according to various group structures, from 175 to 709 groups.

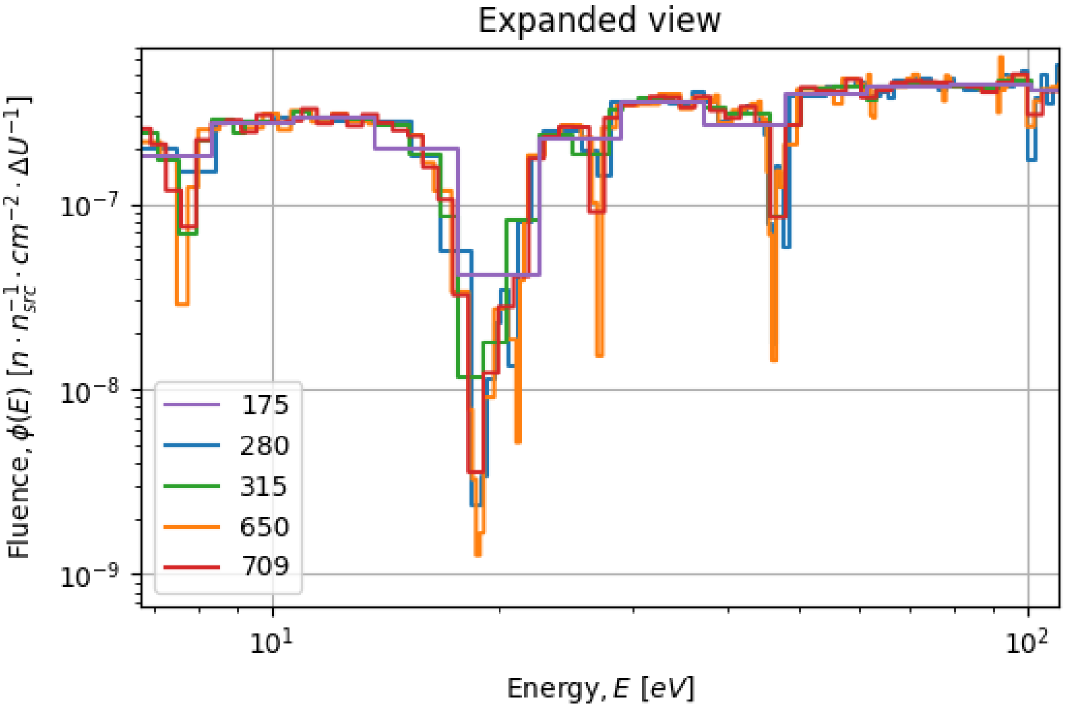

Fig. 4.3 Magnified section of spectrum showing how progressively finer group structures resolve flux depressions in a neutron spectrum.

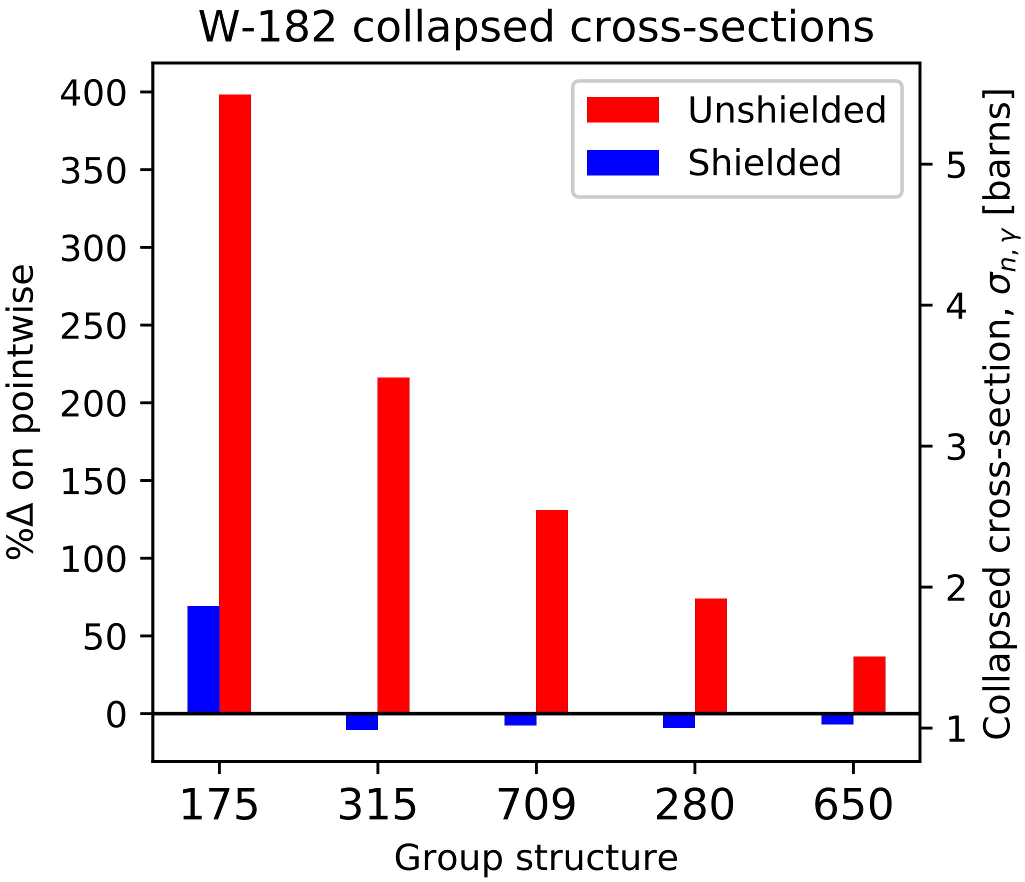

Fig. 4.4 Comparison of different calculation methods for radiative capture in ^{182}W under JET neutron irradiation.

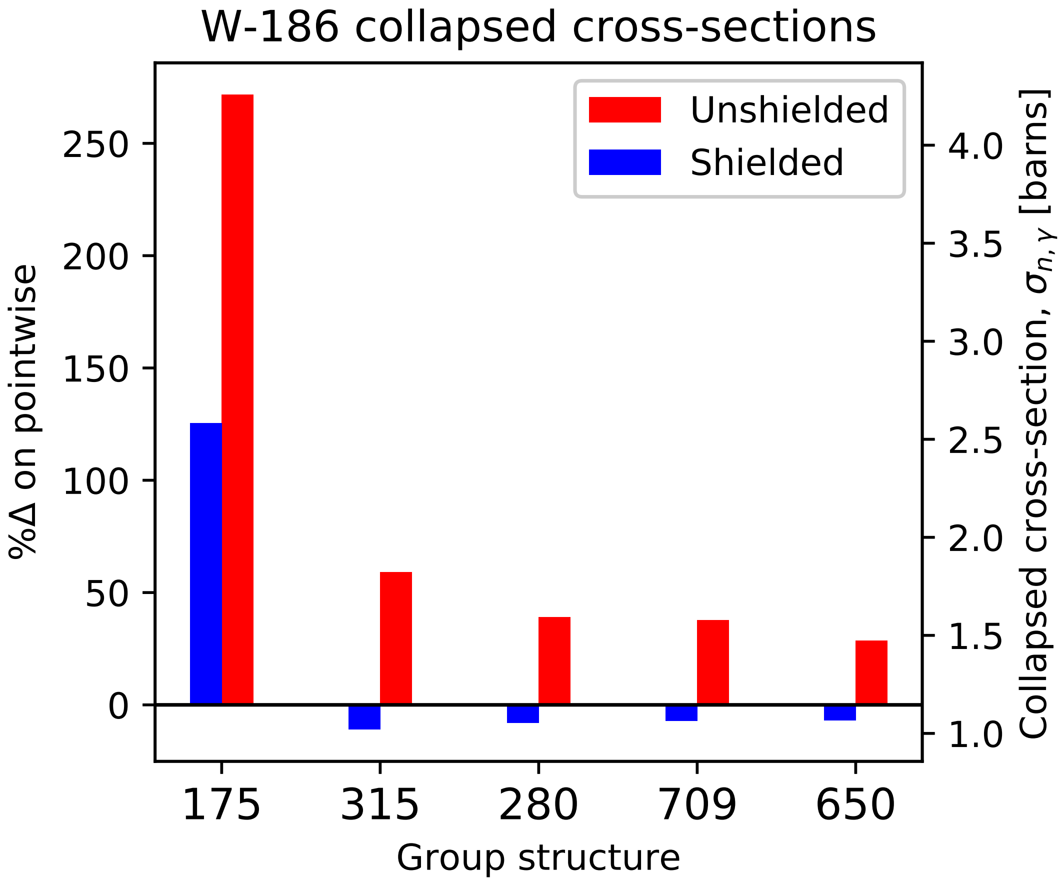

Fig. 4.5 Comparison of different calculation methods for radiative capture in ^{186}W under JET neutron irradiation.

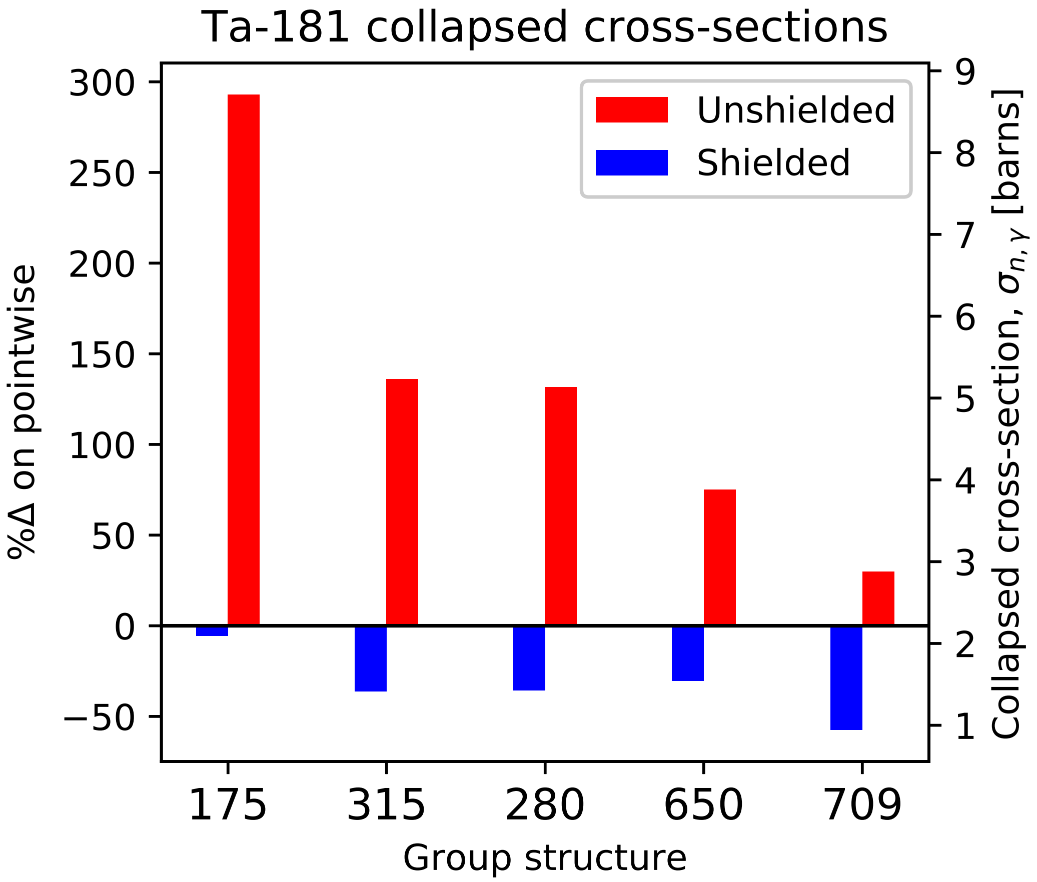

Fig. 4.6 Comparison of different calculation methods for radiative capture in ^{181}Ta under JET neutron irradiation.

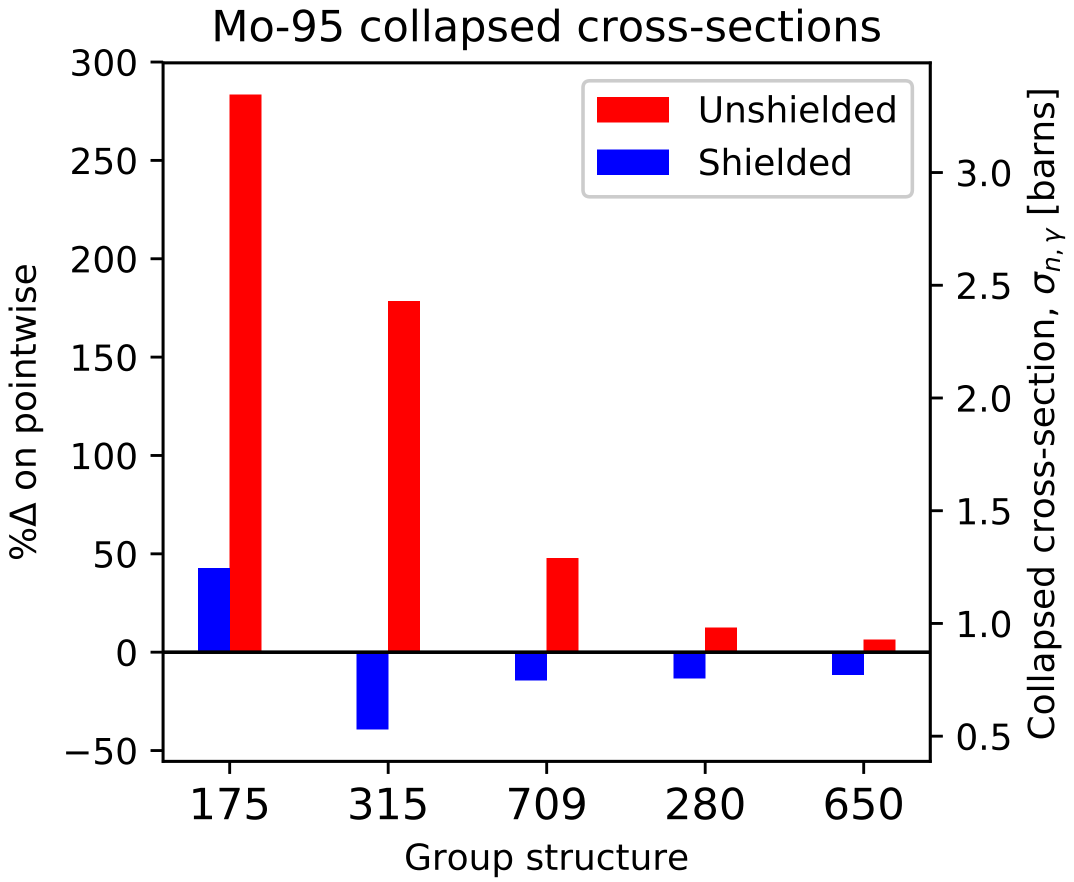

Fig. 4.7 Comparison of different calculation methods for radiative capture in ^{95}Mo under JET neutron irradiation.

Chapter 5

Concluding remarks

5.1 Comparison of sources of uncertainty studied

5.2 Recommendations for neutronics practitioners

5.3 Recommendations for further research

References

[1] Akbari, M., Khoshahval, F., Minuchehr, A., and Zolfaghari, A. (2013). A novel approach to find optimized neutron energy group structure in MOX thermal lattices using swarm intelligence. *Nuclear Engineering and Technology*, 45(7):951–960.

[2] Akbari, M., Minuchehr, A., Zolfaghari, A., and Khoshahval, F. (2012). An investigation for an optimized neutron energy-group structure in thermal lattices using Particle Swarm Optimization. *Annals of Nuclear Energy*, 47:53–61.

[3] El-Guebaly, L. a. and Malang, S. (2009). Toward the ultimate goal of tritium self-sufficiency: Technical issues and requirements imposed on ARIES advanced power plants. *Fusion Engineering and Design*, 84(12):2072–2083.

[4] Fischer, U., Bachmann, C., Palermo, I., Pereslavtsev, P., and Villari, R. (2015). Neutronics requirements for a DEMO fusion power plant. *Fusion Engineering and Design*, pages 2–5.

[5] Fleming, M. J., Morgan, L. W. G., and Shwageraus, E. (2016). Optimization Algorithms for Multigroup Energy Structures. *Nuclear Science and Engineering*, 183:173–184.

[6] Goorley, T., James, M., Booth, T., Brown, F., and Bull, J. (2012). Initial MCNP6 Release Overview. *Nuclear Technology*, 180(3):298–315.

[7] Koning, A. J. and Rochman, D. (2008). Towards sustainable nuclear energy: Putting nuclear physics to work. *Annals of Nuclear Energy*, 35:2024–2030.

[8] Leichtle, D., Fischer, U., Perel, R. L., and Serikov, A. (2011). Sensitivity and uncertainty analysis of nuclear responses in the EU HCLL TBM of ITER. *Fusion Engineering and Design*, 86(9-11):2156–2159.

[9] Lengar, I. (2017). Private communication.

[10] Morgan, L., Sublet, J.-C., Haeck, W., and Pasley, J. (2013). Optimising the energy group structure used for fusion systems. *Annals of Nuclear Energy*, 55:108–115.

[11] Rhodes, J., Smith, K., and Lee, D. (2006). CASMO-5 development and applications. In *Proc. ANS Topical Meeting on Reactor Physics*.

[12] Rising, M. E. (2012). *Quantification and Propagation of Nuclear Data Uncertainties*. PhD thesis, University of New Mexico.

[13] Rochman, D., Koning, A. J., Sublet, J. C., Fleming, M., Bauge, E., Hilaire, S., Romain, P., and Morillon, B. (2016). The TENDL library: hope, reality and future. In *ND 2016 International Conference on Nuclear Data for Science and Technology*.

[14] Rochman, D., Zwermann, W., van der Marck, S., Koning, A. J., Sjostrand, H., Helgesson, P., and Krzykacz-Hausmann, B. (2014). Efficient Use of Monte Carlo: Uncertainty Propagation. *Nuclear Science and Engineering*, 177:337–349.

[15] Sublet, J.-C. (2011). CALENDF-2010: USER MANUAL. Technical report, CEA Saclay.

[16] Sublet, J.-C., Eastwood, J. W., Morgan, J. G., Fleming, M., and Gilbert, M. R. (2015). The FISPACT-II User Manual. Technical Report 6, UK Atomic Energy Authority.

[17] Yi, C. and Sjoden, G. (2013). Energy group structure determination using particle swarm optimization. *Annals of Nuclear Energy*, 56:53–56.